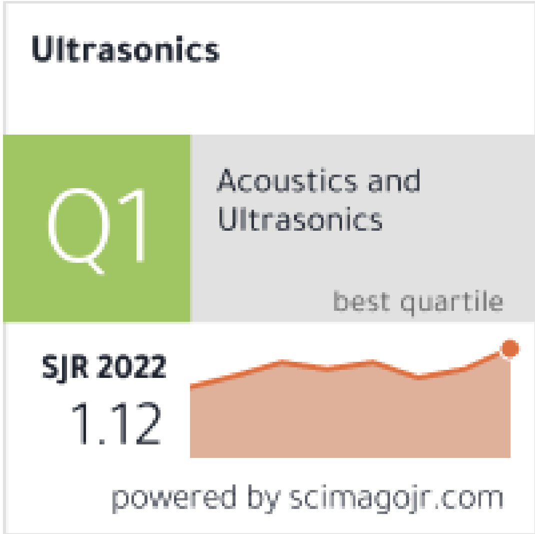

Ultrasonics

COUNTRY

Netherlands

Universities and research institutions in Netherlands

Media Ranking in Netherlands

SUBJECT AREA AND CATEGORY

Physics and Astronomy
└ Acoustics and Ultrasonics

PUBLISHER

Elsevier

H-INDEX

105

PUBLICATION TYPE

Journals

ISSN

18749968, 0041624X

COVERAGE

1963-2023

INFORMATION

Homepage

How to publish in this journal

Contact

SCOPE

Ultrasonics is the only internationally established journal which covers the entire spectrum of ultrasound research, technology and applications. Ultrasonics contains a variety of sections to keep its readers abreast of the state of the art in both fundamental investigation and real-world development related to ultrasonics. Ultrasonics publishes papers of exceptional quality and of relevance to both academia and industry. Manuscripts in which ultrasonics is the core and not simply an incidental tool or secondary issue are welcomed. In addition to high-quality, original research papers with scientific merit and novelty, as well as review articles contributed by internationally renowned experts, Ultrasonics also regularly features short communications, a calendar of forthcoming events in the field, and special issues dedicated to specific topical subjects.

Join the conversation about this journal

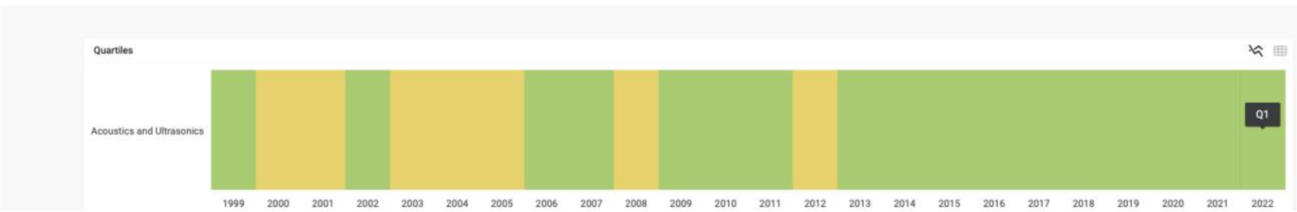

Ultrasonics 132 (2023) 106989

Contents lists available at ScienceDirect

Ultrasonics

journal homepage: www.elsevier.com/locate/ultras

Effects of ultrasonic vibration on microstructure and mechanical properties of 1Cr12Ni3MoVN alloy fabricated by directed energy deposition

Zhen Wang [a], Fengchun Jiang [a,b,*], Chunhuan Guo [a,*], Xiaodong Xing [a], Zhenlin Yang [b], Haixin Li [b], Chuanming Liu [a], De Xu [a], Guorui Jiang [a], Sergey Konovalov [b,c]

[a] Key Laboratory of Superlight Materials & Surface Technology, Ministry of Education, College of Materials Science and Chemical Engineering, Harbin Engineering University, Harbin 150001, China
[b] Yantai Research Institute and Graduate School of Harbin Engineering University, Yantai 264006, China
[c] Siberian State Industrial University, 42 Kirov Street, Novokuznetsk 654007, Russia

ARTICLE INFO

Keywords:
Directed energy deposition
Ultrasonic vibration
1Cr12Ni3MoVN alloy
Microstructure and mechanical properties

ABSTRACT

Due to the rapid melting and solidification during directed energy deposition (DED) process, the defects and columnar crystals are likely to generate in the deposition layers, which reduce the quality and performance of the whole parts. Therefore, in order to improve the microstructure and mechanical properties of 1Cr12Ni3MoVN alloy manufactured by DED method, ultrasonic vibration (UV) has been employed to assist directed energy deposition process in this work. The results indicate that the high-intensity ultrasonic vibration can weaken the epitaxy growth tendency of crystal grains, and significantly improve plasticity while keeping an approximate strength. In addition, a two-dimensional numerical model is established to simulate the effect of ultrasonic vibration in the molten pool. The simulation results show that ultrasonic vibration remarkably improves the flow velocity and pressure in the molten pool, inducing the cavitation effect that breaks dendritic crystal and affects crystal characteristics. Meanwhile, the acoustic streaming effect changes the thermodynamic conditions and promotes high-temperature diffusion, which uniforms temperature distribution and reduces the temperature gradient in the molten pool. Thus the reduced temperature gradient G and raised solidification growth rate R promote the formation of fine equiaxed crystal characteristics after UV treatment. The product G × R increases and the ratio G/R decreases after UV treatment, resulting in the formation of fine equiaxed crystals.

1. Introduction

Laser-based directed energy deposition (DED), as a kind of additive manufacturing (AM) process, takes both precision forming and high performance into consideration to manufacture complex structural parts. The process melts powders by laser beam to build parts layer-by-layer according to the CAD file of digitized geometry[1]. DED has been applied to manufacture parts in many fields including aerospace and marine equipment[2–5]. Due to the rapid melting and solidification during the process of DED, it is likely to create some defects in the parts, such as porosity[6]. Besides, the high temperature gradient in the molten pool and the thermal cycle are also the reasons to form the coarse columnar crystals in the components.[7]. The defects and coarse columnar crystals reduce the quality and mechanical properties of parts, and limit the application of the DED technique in the industrial fields. Thus, it's necessary to investigate the techniques to reduce defects and improve the mechanical properties of components in situ.

The methods to improve microstructure and properties of additive manufactured parts including material design[8], reinforcing particles [9], offline postprocessing[10–12], ultrasonic vibration[13–21], and rolling[22,23] have been proposed until now. With the effect of ultrasonic cavitation and acoustic streaming in the molten pool[20,24–27], ultrasonic vibration (UV) technology regulates the metal solidification process to refine grain, uniform structure, and reduce defects on the deposition layer. Todaro et al.[13] found equiaxed prior-β grains formed with a small grain size (~100 μm) and a low grain aspect ratio in the samples prepared by ultrasonic-assisted DED. The ultrasound intensity within the deposition layer was calculated, which is far greater than the threshold for acoustic cavitation, confirming the effect of cavitation on grain refinement. Moreover, Yang et al.[14] established a kinetic model

* Corresponding authors at: Key Laboratory of Superlight Materials & Surface Technology, Ministry of Education, College of Materials Science and Chemical Engineering, Harbin Engineering University, Harbin 150001, China (F. Jiang).
E-mail addresses: fengchunjiang@hrbeu.edu.cn (F. Jiang), guochunhuan@hrbeu.edu.cn (C. Guo).

https://doi.org/10.1016/j.ultras.2023.106989
Received 8 November 2022; Received in revised form 16 February 2023; Accepted 20 March 2023
Available online 25 March 2023
0041-624X/

of powder flow based on the gas–solid fluid mechanics and confirmed that the cavitation bubble affects the Marangoni flow in the molten pool and accelerates the escape of bubbles. Besides, the impact force produced by cavitation bubbles destroys the growth of columnar crystals, and the thermodynamic conditions during solidification are also changed due to the cavitation and acoustic flow, which leads to the increase of nucleation rate and the change of microstructure. In addition, the synchronous couple ultrasonic vibration technique verified by experiment and simulation demonstrated that the acoustic cavitation effect produced by high-intensity ultrasound is an important factor that refines grains[15]. Up to now, various additive manufacturing methods in which the ultrasonic vibration was introduced into the molten pool have been developed to improve the microstructure and enhance the mechanical properties of components. For example, Zhou et al.[16] utilized non-contact ultrasound to refine the grains from 0.8 μm to 0.4 μm in the DED process, accompanied by an increase in elongation from 6% to 12%. Yuan et al.[25] put an ultrasonic probe into the weld pool to stir the pool, which received an excellent effect in grain refinement due to a greater ultrasonic amplitude achieved. In the most of studies performed, the ultrasonic vibration was introduced to the molten pool from the bottom of the substrate[13,14,17,18,20] or the behind of the molten pool[15,19,21]. While it is confirmed that both cases have some limitations. For the first cases, due to the attenuation of ultrasound during transmission, the effect of ultrasonic vibration on the solidification during AM process is weakened with increasing component height. For the later cases, the distance from the ultrasonic probe to the molten pool is an important factor that affects the effect of ultrasonic vibration. When this distance is too far, the effect of ultrasonic vibration becomes weaker due to the attenuation of ultrasound and the low temperature of the deposited layer. While if the ultrasonic probe is too close to the molten pool, the ultrasonic probe is easily damaged by the high temperature and radiation from the molten pool and laser beam.

1Cr12Ni3MoVN (M152) alloy, one of martensitic heat-resistant stainless steel with 12% Cr, has high medium temperature creep resistance, durability, good fatigue, and corrosion resistance, which has been widely used in energy, naval equipment, and other fields[28]. The application of martensitic stainless steel in additive manufacturing has been widely studied, with a focus on precipitation hardened [9,23,29,30], maraging[31–33] and tools steels[34–36], while this heat-resistant steel has received less attention. Due to complex microstructure, defects, and residual stress, the martensitic steel parts manufactured by AM has performance shortcomings including low plasticity[9].

To improve the microstructure and mechanical properties of the AM-fabricated metallic parts, a new ultrasonic vibration method was proposed in this study. Different from the aforementioned techniques, the ultrasonic probe made of tungsten is directly connected with the ultrasonic transducer. Therefore, the ultrasound can be transmitted into the molten pool along the ultrasonic transducer and tungsten needle. The device moves with the laser deposition system at a given distance to ensure that the tungsten needle will not be melted. The newly-developed ultrasonic vibration method has been examined based on the investigation into the microstructure and mechanical properties of 1Cr12Ni3MoVN alloy fabricated by DED process. In addition, the influence of ultrasonic vibration in the molten pool was investigated by the simulation and the numerical calculation. Meanwhile, the mechanisms of grain refinement by UV treatment were discussed based on the experimented and simulated results.

2. Experiments

2.1. Materials

The metal powders used in this experiment were 1Cr12Ni3MoVN martensitic heat-resistant stainless steel with a particle size range of 53–150 μm, and the main chemical compositions of the stainless steel powders were shown in Table 1. The 304 stainless steel plate with a size of 200 mm × 100 mm × 10 mm was used as substrate material.

2.2. Experimental setup

The schematic diagram and experimental setup employed in this investigation are shown in Fig. 1, which includes directed energy deposition (DED) system and ultrasonic vibration (UV) system. The DED system consists of a semi-conductor laser with a maximum output laser power of 6 kW, numerical control table, powder feeder, coaxial powder deposition head, and gas protection device. The UV system includes ultrasonic generator, ultrasonic transducer, ultrasonic horn, and tungsten needle. The max output power of the ultrasonic generator utilized in this work is 1000 W. The ultrasonic horn is tightly connected with the tungsten needle by a special clamp. The tungsten needle contacts with the edge of molten pool at 60 degrees to ensure it will not be melted (as shown in Fig. 1(a)). The ultrasound is transmitted to the molten pool through the tungsten needle and has a continuous effect on the molten metal, in which the frequency and amplitude of ultrasonic are 20 kHz and 20 μm, respectively, similar to the ultrasonic generator. A flexible atmosphere box made by high temperature plastic film is constructed to avoid oxidation of components during deposition.

The working principle of the the directed energy deposition system assisted with ultrasonic vibration is shown in Fig. 1(a). In which the metal powders are sent to the laser spot center by the powder feeder and are molten by the laser. The relative movement of the substrate and the coaxial powder deposition head is controlled by the numerical control table to deposit components. To improve the defects of coarse columnar crystals and residual stress caused by high solidification rate and temperature gradient during the solidification of the molten pool, the ultrasonic vibration is introduced into the molten pool during the directed energy deposition process in the paper. The cavitation and acoustic streaming generated by the ultrasonic vibration can break dendritic crystals and increase nucleation rate, which can refine grains. The details can be found in Fig. 1(a). The ultrasound generated by the ultrasonic generator is transferred to the molten pool by the tungsten needle that is installed at the front of the deposition head and is directly contacted with the molten pool.

During deposition, four different ultrasonic powers of 0 W, 200 W, 600 W, and 1000 W were employed, while the other ultrasonic vibration parameters that include frequency and amplitude were identical, they are 20 kHz in frequency and 20 μm in amplitude. The DED processing parameters were as follows: laser power ~ 2400 W, scanning speed ~ 10 mm/s, powder feeding rate ~ 20 g/min, and argon gas flow rate ~ 15 L/min. The thin walls with 5 layers were deposited for microstructure observation and 20 layers were for tensile machining specimens.

2.3. Microstructure characterization and mechanical testing

An optical microscope (ZEISS Axioscope 5) and a scanning electron microscope (Hitachi S-3000 N) were used to characterize the microstructural features of all samples fabricated by DED process along Y-Z plane. According to ASTM standards, the Vickers hardness test was

Table 1
Chemical compositions of 1Cr12Ni3MoVN powder (wt.%).

Fe	C	Si	Mn	P	S	Ni	Cr	N	Mo	V
Bal.	0.11	0.23	0.77	0.021	0.002	2.69	11.41	0.031	1.58	0.28

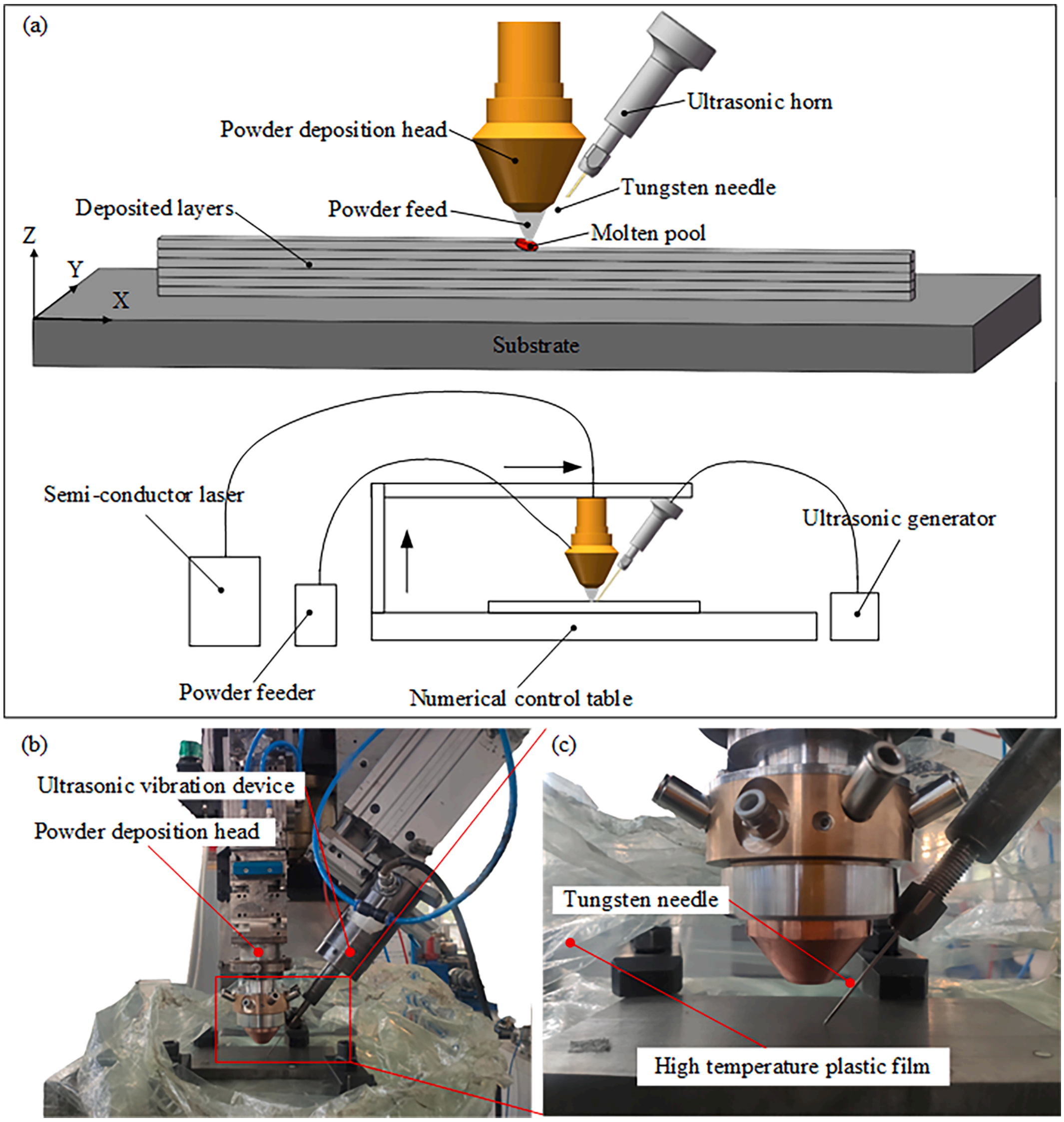

Fig. 1. (a) Schematic diagram of directed energy deposition system assisted with ultrasonic vibration, (b) Experimental setup of directed energy deposition system assisted with ultrasonic vibration, (c) Local magnification of deposition head and tungsten needle.

conducted at a 500 g load with a dwell time of 15 s. The measure points were taken from the top to the bottom of the sample with an interval of 150 μm, and each point was measured three times to get the average value. The thin walls were machined into tensile specimens in the XZ plane with a section size of 2.5 mm × 4 mm and a gauge length of 25 mm. Tensile testing was performed three times per condition with a loading speed of 0.5 mm/min using the MTS EXCEED E43 instrument equipped with a contacting extensometer at room temperature.

3. Experimental results and analysis

3.1. Microstructures

Fig. 2 shows the intralayer microstructures (Y-Z plane) of 1Cr12Ni3MoVN alloy samples fabricated by DED with different ultrasonic powers. The microstructures mainly contain martensite and δ-ferrite phase, in which the δ-ferrite distributes along the grain boundary. The microstructure of the sample without UV (the ultrasonic power is 0 W) consists of coarse columnar crystals that grow along the Z axis (see Fig. 1(a) for details), which is dependent upon the great temperature gradient and low cooling rate during the DED process. Generally, the columnar crystals lead to solidification defects and mechanical property anisotropy[37]. Therefore, it is desirable to convert the columnar into equiaxed for improving mechanical properties. It is noted from Fig. 2(a)-(d) that with increasing ultrasonic power, the microstructure growth tendency becomes more disorganized, and the columnar crystal transforms into equiaxed crystal gradually. When the ultrasonic power is up to 1000 W, the columnar growing tendency disappears with the microstructure of fine equiaxed crystal as shown in Fig. 2(d).

Fig. 3 shows the interlayer microstructures (Y-Z plane) of 1Cr12Ni3MoVN alloy samples fabricated by DED with different ultrasonic powers. Clearly, equiaxed crystal characteristics are observed in the interlayer microstructure of all the samples, and the grain size decreases with increasing ultrasonic power. The average grain sizes and grain sizes distribution measured by Image Pro Plus software are shown in Fig. 4. It is noted that the average area size of grains is reduced from 158 μm^2 to 80 μm^2 when the ultrasonic power is changed from 0 W to 1000 W. During the DED process, since the cooling rate of molten pool surface is quite fast, there is no enough time for the grains to grow up, which results in the grain refinement. Therefore, the microstructure at the top of deposited layer shows fine equiaxed crystal characteristics. When depositing the next layer, the part of the previously-deposited layer is remelted, while the rest, namely the unmelted interlayer, still

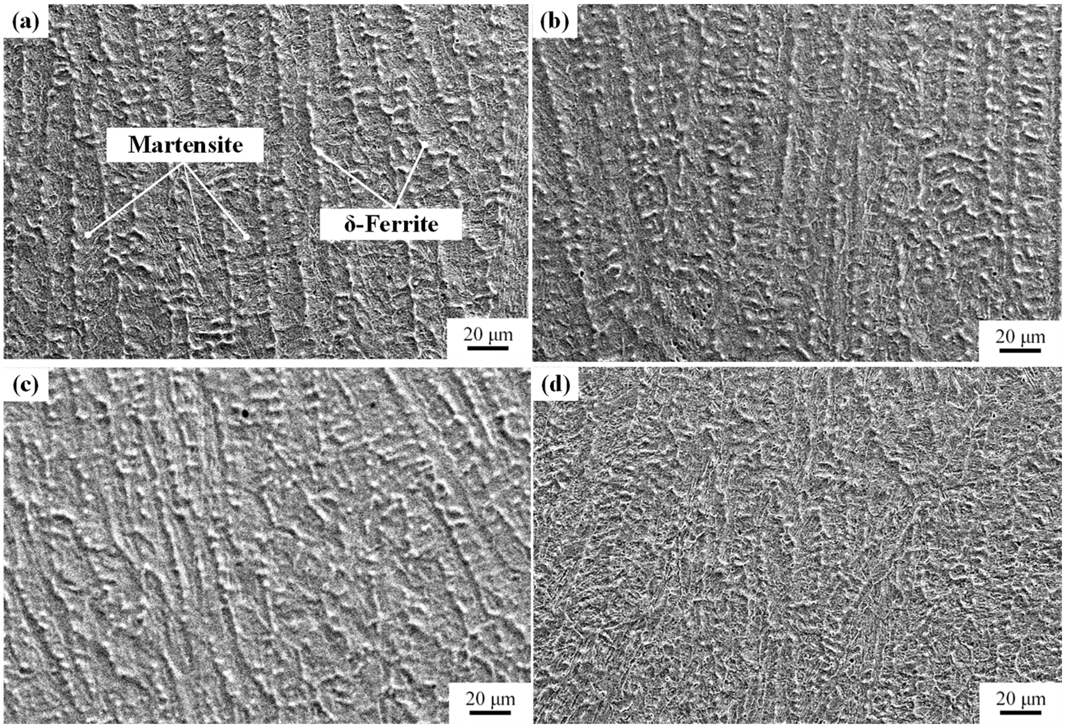

Fig. 2. Intralayer microstructures of 1Cr12Ni3MoVN alloy samples at different ultrasonic powers: (a) 0 W, (b) 200 W, (c) 600 W, (d) 1000 W. Here the laser power is 2400 W, the scanning speed is 10 mm/s, and the powder feeding rate is 20 g/min.

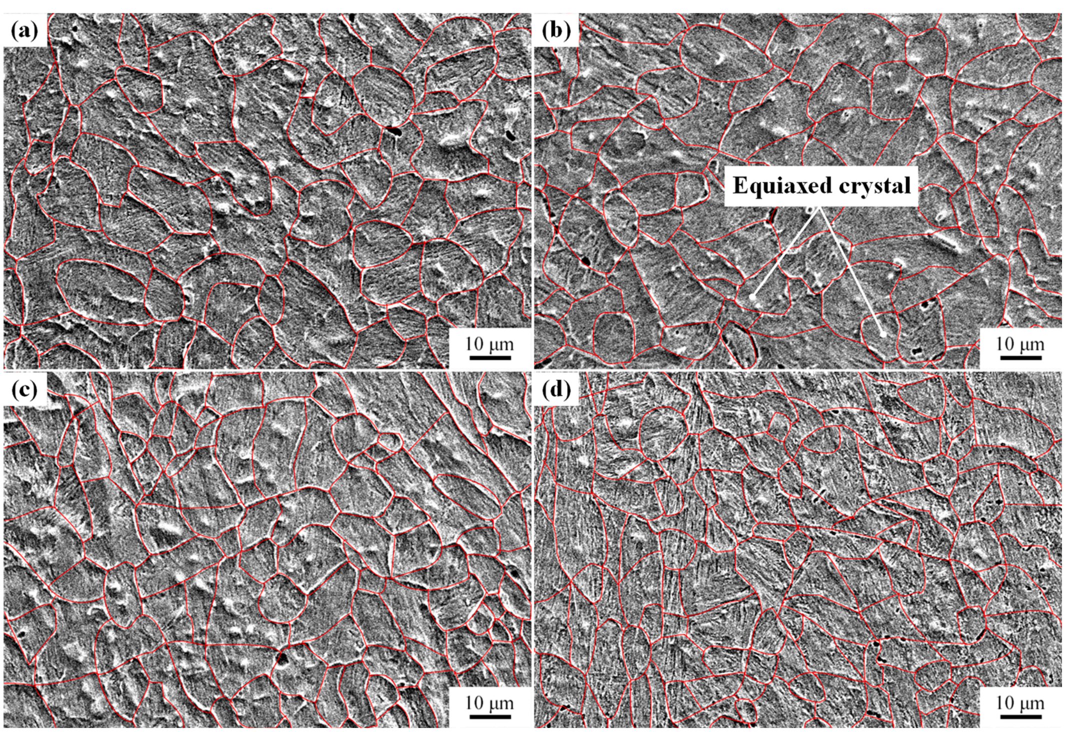

Fig. 3. Interlayer microstructures of 1Cr12Ni3MoVN alloy samples at different ultrasonic powers: (a) 0 W, (b) 200 W, (c) 600 W, (d) 1000 W. Here the laser power is 2400 W, the scanning speed is 10 mm/s, and the powder feeding rate is 20 g/min.

remains equiaxed crystal.

3.2. Mechanical properties

Fig. 5 displays the microhardness distribution of four samples deposited by DED with different ultrasonic powers. It is worth bearing in mind that the microhardness of the sample treated by UV with an ultrasonic power of 200 W has an evident increase, and the average microhardness is around 521 HV that is higher than that without UV treatment. With increasing ultrasonic power, the average microhardness decreases. The average microhardness of the sample treated with UV at 1000 W is the lowest, which is 446 HV lower than that treated with 200

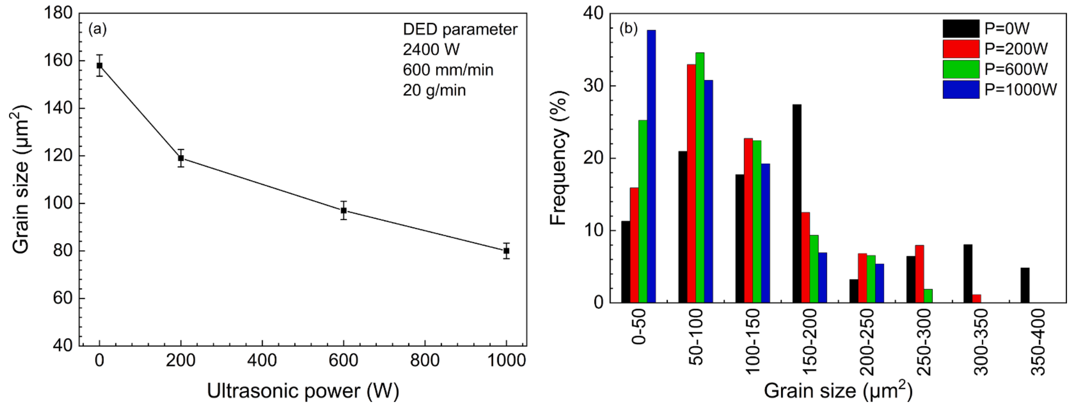

Fig. 4. The area sizes of interlayer grain under different ultrasonic powers: (a) Average area sizes of grain, (b) Area sizes distribution of grain.

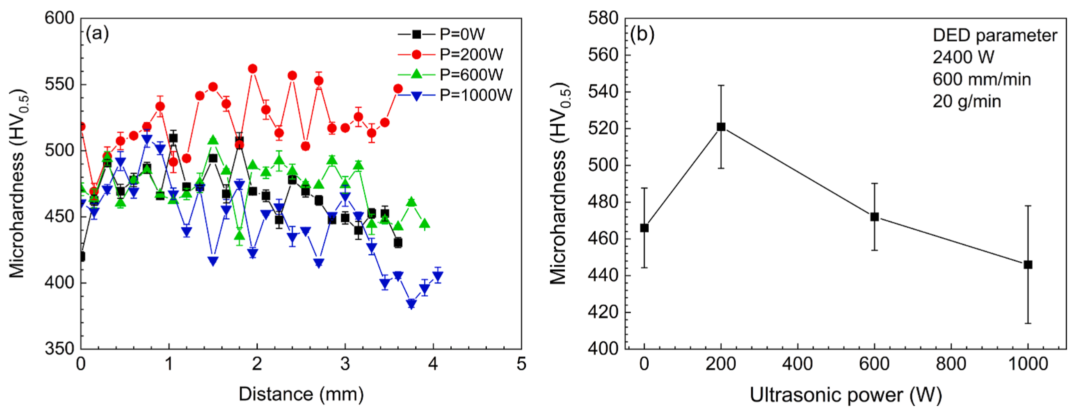

Fig. 5. Microhardness variations of 1Cr12Ni3MoVN alloy samples deposited with different ultrasonic powers: (a) Microhardness distribution from the top of sample to bottom, (b) Variation of the average microhardness as a function of ultrasonic power.

W. Besides, it can be found that the microhardness of samples with different ultrasonic powers is similar at the top of the deposited thin wall. This is related to the rapid cooling of the deposited layer surface without remelting and rapid heat treatment, which weakens the effect of ultrasonic vibration. Therefore, the top areas of samples deposited at different processing parameters show a similar microstructure with all fine equiaxed grains, leading to the similar microhardness of samples at different ultrasonic powers, detailed microhardness distribution can be found between the distance of 0–1 mm, as shown in Fig. 5(a).

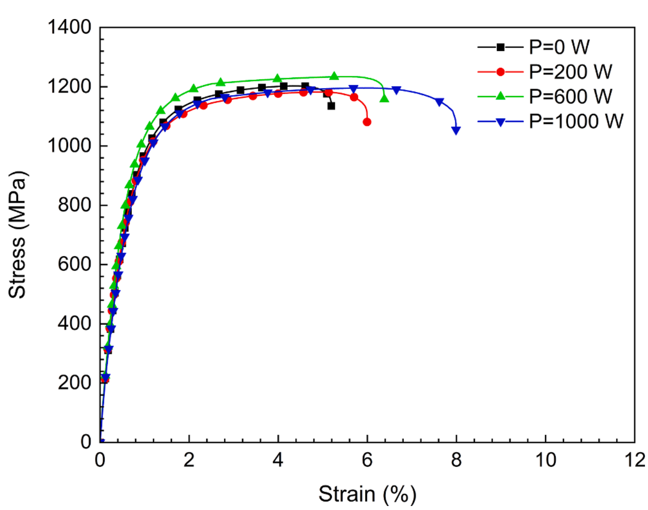

Fig. 6. Typical tensile stress–strain curves of samples deposited with different ultrasonic powers, in which the powers are 0 W, 200 W, 600 W and 1000 W.

The stress–strain curves of DED 1Cr12Ni3MoVN alloy are shown in Fig. 6, and the corresponding tensile properties are summarized in Table 2. The ultimate tensile strength of samples treated with different ultrasonic powers is almost identical and the difference between the maximum and the minimum is only within ~ 3%, while the elongation of samples treated with different ultrasonic powers shows considerable difference, it increases with increasing ultrasonic power. The elongation of samples at 1000 W is increased by 53.8% compared with that deposited at 0 W. Meanwhile, the product of strength and elongation (PSE)[38] is improved by 52.9%, meaning that the ultrasonic vibration treatment is an effective way to improve the toughness of 1Cr12Ni3-MoVN alloy manufactured by DED.

Fig. 7 shows the fracture morphology of tensile samples without and with ultrasonic treatment. It can be seen in Fig. 7(a) that except the ductile fracture characteristics (dimples), some tear ridges are visible in the samples without ultrasonic treatment, which are typical quasi-

Table 2
Tensile properties of DED 1Cr12Ni3MoVN samples.

Ultrasonic power (W)	YS (MPa)	UTS (MPa)	EL (%)	Product of strength and plasticity (GPa%)
0	828 ± 34	1202 ± 28	5.2	6.25
200	819 ± 30	1182 ± 12	6	7.09
600	820 ± 35	1234 ± 25	6.4	7.90
1000	787 ± 40	1195 ± 34	8	9.56

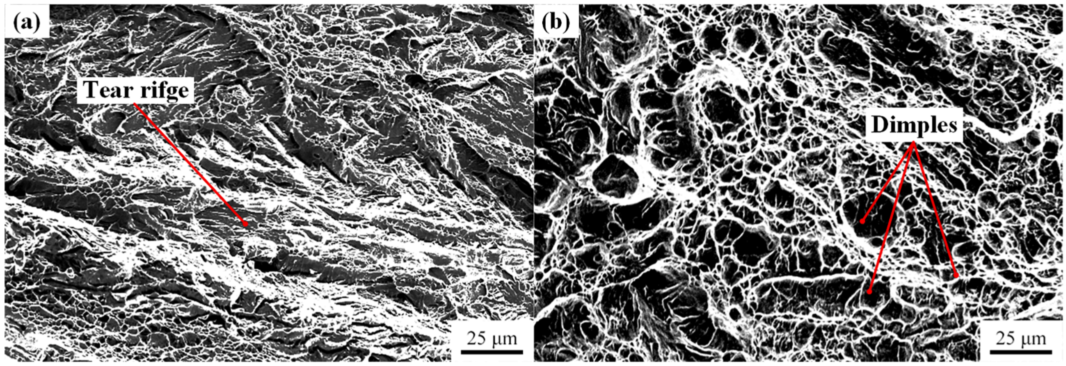

Fig. 7. Fracture morphology of 1Cr12Ni3MoVN alloy samples without and with ultrasonic treatments: (a) Without ultrasonic, (b) With ultrasonic at 1000 W.

cleavage fracture characteristics. As can be seen in Fig. 7(b), while plenty of deep dimples can be found from the fractured surface of the sample treated by 1000 W UV. Clearly, a pure ductile fracture takes place in the UV treated sample under tensile loading, implying the UV improves the plasticity of the deposited sample.

4. Simulations and discussion

It has been reported that when the UV is applied from the bottom of the substrate, the molten pool on the top of the substrate is affected by the UV, and the fluid velocity and pressure of the molten pool rise, accelerating the cooling rate of the molten pool and creating cavitation bubbles in the pool[20]. When the diameters of bubbles reach the critical threshold, they implode and generate instantaneous high pressure in the molten pool, and create dendrites to break and grain to refine. To verify the effect of the UV in the current experiment, in which the ultrasound is directly transmitted into the molten pool through a tungsten needle, the fluid velocity and pressure distribution of the molten pool were simulated by the COMSOL Multiphysics software.

Fig. 8 shows the model calculation domain and boundary conditions of the two-dimensional model used in this study. It contains fluid domain (molten pool) and solid domain (deposited layer). The velocity and pressure of the fluid are calculated by the Turbulent Flow module, and the thermal state of the model is calculated by the Heat Transfer module. To couple fluid flow and heat transfer, a Non-Isothermal Flow module is added to the model. The ultrasonic vibration is introduced into the fluid domain by applying sinusoidal displacement to the boundary (3) according to Eq. (1)

$$A(t) = A_0 \sin 2\pi f t \tag{1}$$

where A_0 and f are the amplitude (20 μm) and frequency (20 kHz) of the ultrasonic generator, respectively. To simplify the model, the temperature of deposited layer boundaries (5), (6) and pool surfaces (2), (3) are set to 873 K and 2273 K independently, then the initial temperature of the model is obtained by stationary study. The pool surface temperature boundaries will be removed in the dependent study. The thermal convection and radiation are considered at model surfaces (1)-(3). In addition, the Phase Change Materials are added to the Heat Transfer module to track the solid–liquid interface during solidification.

Fig. 9 shows the tendency of pressure at point A (see Fig. 8) with and without UV. Here point A is in the front and close to the tip of the tungsten needle. When the ultrasonic vibration travels in the molten pool, sinusoidal pressure will be created in the molten pool, contributing to the compression and expansion of the bubbles in the liquid. If the negative pressure exceeds the threshold of cavitation, the bubbles will burst and generate a shock wave, which will impact the crystallization

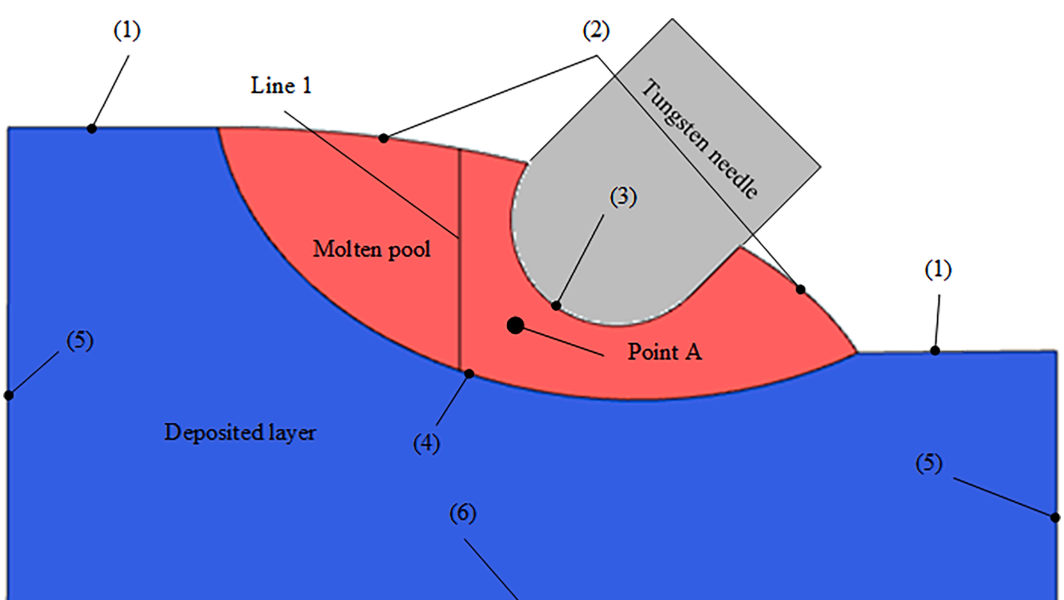

Fig. 8. Calculation domain and boundary conditions of the modeling geometry: (1) Top surface of deposited layer with thermal convection and radiation; (2) Top surface of the molten pool with 2273 K, thermal convection and radiation; (3) Tungsten needle boundary with sinusoidal displacement according to Eq. (1); (4) Solid-liquid interface as phase change interface, (5) and (6) Deposited layer boundary with 873 K.

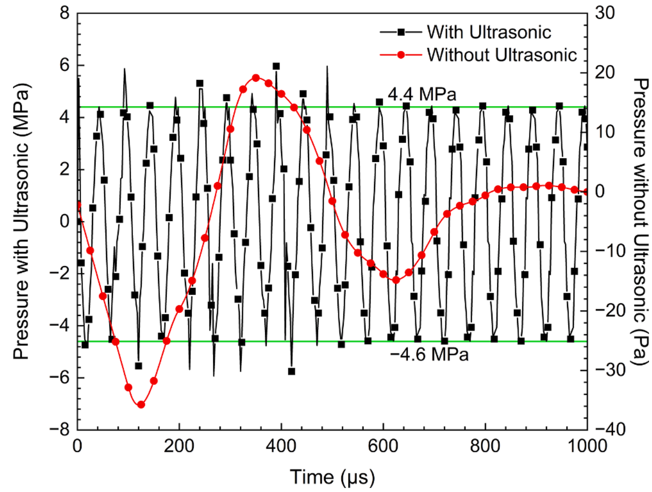

Fig. 9. Variation of sound pressure at point A as a function of time.

and the growths of the grains during the solidification of the molten pool, and break the previously-formed columnar grains into quantities of crystallites[20]. The crystallites can be used as nucleation points of the later crystalline to refine the grains. The threshold value of ultrasonic cavitation in the molten pool is calculated as follows[39]:

$$P_B = P_0 - P_v + \frac{2}{3\sqrt{3}}\left[\frac{\left(\frac{2\sigma}{R_0}\right)^3}{P_0 - P_v + \frac{2\sigma}{R_0}}\right]^{\frac{1}{2}} \tag{2}$$

where P_0 (0.1013 MPa) is the liquid static pressure, P_v (0 Pa) is the saturation vapor pressure, σ stands for the surface tension coefficient of 1Cr12Ni3MoVN alloy molten pool, which is calculated by Eq. (3) to be 1.72 N/m at 2000 K, and R_0 (10 μm) is the initial radius of the bubble. The corresponding cavitation threshold P_B in 1Cr12Ni3MoVN alloy is determined to be ~ 0.278 MPa. It should be noted from Fig. 9 that the max pressure (-4.6 MPa to 4.4 MPa) at point A exceeds the cavitation threshold of cavitation bubbles (P_B). Thus the cavitation effect takes place in the solidification at point A.

Eq. (3) is used to calculate the surface tensions of stainless steels, and the calculated values are within 3% of the measured values[40].

$$\gamma(\mathrm{mNm}^{-1}) = 1840 - 0.4(T - 1823) - 0.056T\ln\left[1 + e^{\frac{28798}{T} - 8.5647}(h_S\%\mathrm{S})\right] \tag{3}$$

where T (K) is the calculated temperature, h_S is the henrian activity coefficient of S in the steel, which is taken to be 0.78 for martensitic steel [40], and the %S is the S content, which is 0.002 for this steel.

To verify whether the cavitation effect occurs in the whole molten pool, the sound pressure distribution in the molten pool during an ultrasonic cycle is extracted from the simulated results, as shown in Fig. 10. The contours represent the part where pressure is higher than the cavitation threshold. When the ultrasonic amplitude reaches the maximum at 12.5 μs and the minimum at 37.5 μs respectively, almost the whole molten pool satisfies the condition of ultrasonic cavitation, and the pressure alternates between positive and negative. Though the ultrasonic amplitude is zero at 25 μs and 50 μs, the top of the tungsten needle also can produce ultrasonic cavitation. In a word, the ultrasonic cavitation can be generated in almost the entire molten pool during a whole ultrasonic period.

The cavitation bubbles generated in the molten pool are compressed and expanded under the alternating pressure. To study the oscillation of cavitation bubbles (the motion low of the bubble wall under the alternating pressure field), the bubble radius, velocity, and pressure at the bubble wall were calculated by Gilmore model[26,41],

$$R\ddot{R}\left(1 - \frac{\dot{R}}{C}\right) + \frac{3}{2}\dot{R}^2\left(1 - \frac{\dot{R}}{3C}\right) = H\left(1 + \frac{\dot{R}}{C}\right) + \frac{R\dot{H}}{C}\left(1 - \frac{\dot{R}}{C}\right) \tag{4}$$

$$C = C_\infty\left(\frac{P + B}{P_\infty + B}\right)^{\frac{n-1}{2n}} \tag{5}$$

$$H = \frac{n(P_\infty + B)}{(n-1)\rho_\infty}\left[\left(\frac{P + B}{P_\infty + B}\right)^{\frac{n-1}{n}} - 1\right] \tag{6}$$

$$P = \left(P_0 + \frac{2\sigma}{R_0}\right)\left(\frac{R_0}{R}\right)^{3\gamma} - \frac{2\sigma}{R} - \frac{4\mu\dot{R}}{R} \tag{7}$$

where R, C, H, and P are the radius, local sonic velocity of the liquid, enthalpy difference between the liquid at pressure P and pressure P_∞, and the pressure at the bubble wall; μ is the viscosity of 1Cr12Ni3MoVN alloy melt, taking 4.9 Pa•s; B and n are constants that are dependent

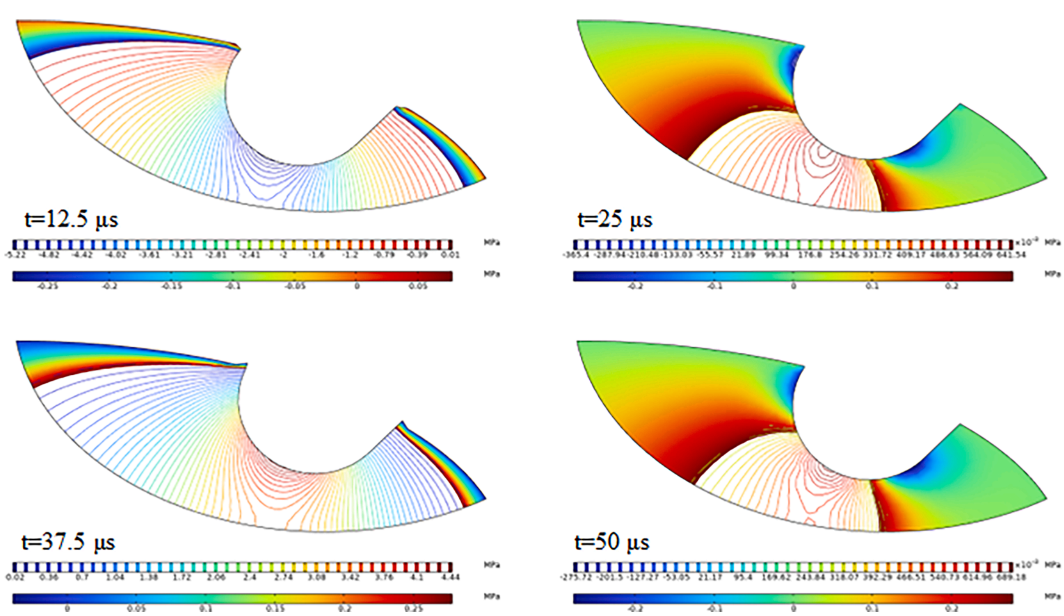

Fig. 10. Pressure distribution in the molten pool during an ultrasonic cycle.

upon the type of liquid, and the value of water at 3000 atm and 7 are employed, respectively; C_∞ is the ambient sound speed in liquid, taking 4200 m/s; γ is the gas polytropic exponent, taking 1.4; and $P_\infty = P_0 + P_a$ is the pressure at infinite distance from the bubble, $P_a = 4.5\cos(2\pi ft)$ MPa at point A according to Fig. 9. The calculation was carried out by COMSOL Multiphysics software, and the calculated result was shown in Fig. 11. The bubble expands and contracts with the pressure variation alternately, resulting in the abrupt change of the velocity and pressure at the bubble wall. The velocity of the bubble wall changes rapidly from − 200 m/s to + 100 m/s with the maximum pressure at the bubble wall of 6 MPa, which will uniform temperature distribution in the molten pool and break dendrites.

Fig. 12 presents the velocity at point A with and without UV treatments. It is noted that the velocity is only 10^{-4} m/s due to the influence of the temperature gradient. When the ultrasonic is introduced into the molten pool, the velocity dramatically increases to 2.6 m/s, indicating that ultrasonic vibration can accelerate the molten pool flow. Besides, the shock wave generated by bubbles burst also increases the local velocity of molten (as shown in Fig. 11(b)). The combination of these two effects will produce acoustic streaming, which ensures the temperature distribution of the molten pool more uniform and speeds up the solidification of the molten pool. To verify whether the temperature distribution is more uniform and the solidification of the molten pool is quicker at the condition of the UV treatment, the distribution of temperature in the molten pool without and with UV is analyzed as shown in Fig. 13. It can be seen from Fig. 13 that the temperature contours are sparser with UV than those without UV. In addition, the maximum temperature in the pool with UV is almost 100 K lower than that without UV. The solidification time of the molten pool without and with UV treatment is 0.074 s and 0.047 s respectively. To further investigate the effect of UV on the molten pool, the temperature gradient in the molten pool along Line 1 (see Fig. 8) is calculated and shown in Fig. 14(a). It is noted that the temperature gradient with UV is lower than that without UV. Besides, the temperature gradient is smoother at the center of the molten pool with UV treatment. Therefore, the acoustic streaming caused by UV can uniform the temperature distribution of the molten pool and reduce the temperature gradient effectively during solidification. The nucleation rate N can be expressed by temperature gradient ΔG according to Eq. (8). With decreasing temperature gradient ΔG, the nucleation rate N rises, accompanying the grain is refined. In short, the ultrasonic vibration decreases the temperature gradient, resulting in the increasing nucleation rate and refining grains.

$$N = C \times Pe^{-\frac{\Delta G^{*} + U^{I}}{k_B T}} \tag{8}$$

It has been confirmed that the combination of the temperature gradient G and solidification growth rate R influences the grain morphology and size of the deposition layer. With increasing product G × R, the structures fabricated by DED become finer. Besides, a lower ratio of G/R is in favor of the formation of equiaxed grains[42]. Fig. 14(c) and 14(d) show the G × R and G/R calculated at the liquid–solid interface with and without UV treatment. It is worth bearing in mind that the G × R raises and the G/R reduces after UV treatment, which can reduce columnar grains and refine grains. The simulation results indicate that the microstructure of the deposited layer shows fine equiaxed grain characteristics, which is in good agreement with the experimental observed results as shown in Fig. 2 and Fig. 3.

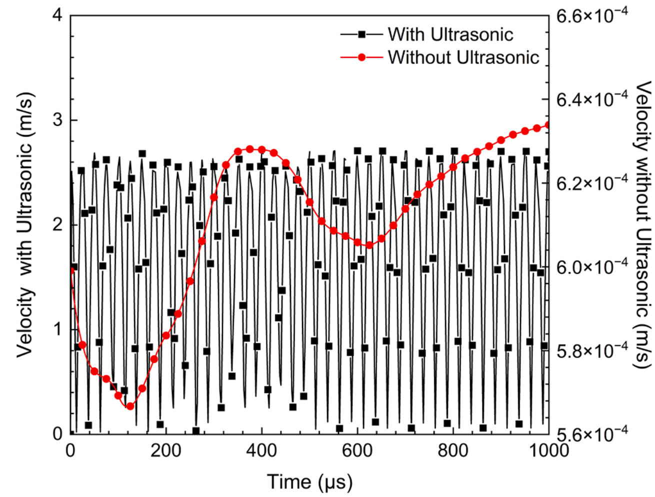

Fig. 12. Variation of velocity of the molten pool at point A as a function of time.

In this study, several potential limitations are found in the current directed energy deposition system assisted with ultrasonic vibration, they are:

(1) The heat is transferred directly from the molten pool to the tungsten needle and the ultrasonic horn, which causes the tungsten needle and the ultrasonic horn heating up rapidly. As a result, the ultrasonic system is hard to work continuously for a long time.

(2) Due to the high local temperature in the molten pool, the front end of the tungsten needle is dissolved, leading to the change of the geometry of the tungsten needle, which affects the resonance frequency and magnification factor of the ultrasonic horn, resulting in the change of the amplitude and frequency of the ultrasound transmitted to the molten pool. Besides, the dissolution of tungsten leads to the change of elements in the samples, which may influence the material properties when the composition changes largely.

(3) In the process of testing other materials, it is found that the tungsten needle can adhere to some materials (such as titanium alloy),

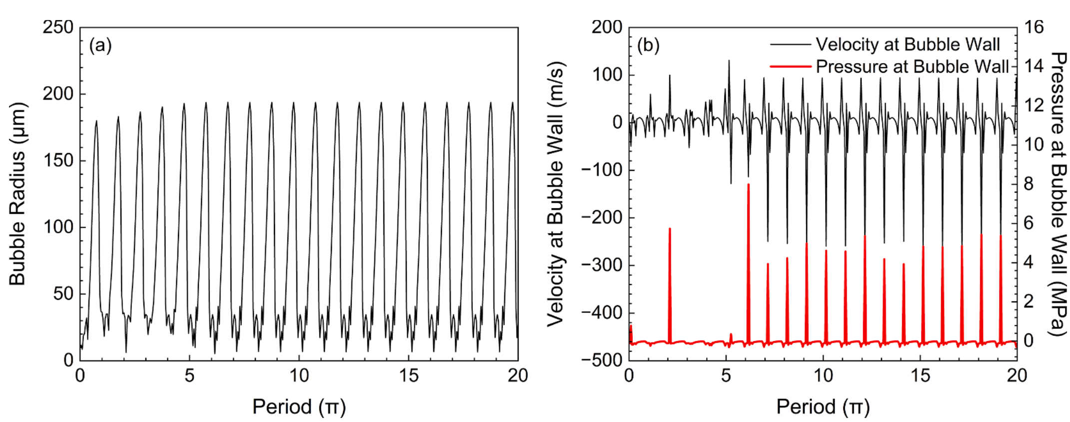

Fig. 11. Oscillation of cavitation bubbles: (a) Variation of the bubble radius under alternating pressure, (b) Velocity and pressure at the bubble wall during cavitation bubbles oscillating.

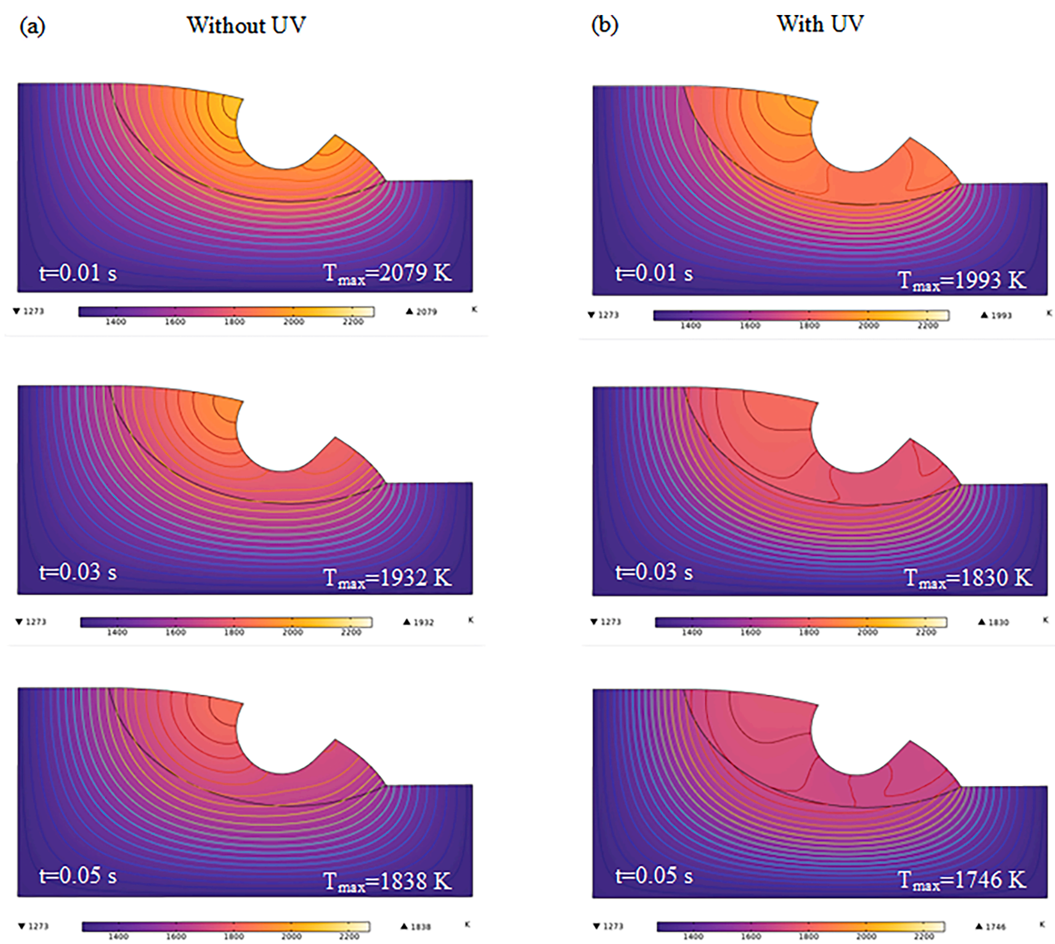

Fig. 13. Variation of temperature distribution in the molten pool at different times: (a) without UV, (b) with UV.

making it difficult to deposit.

Based on the limitations of the system proposed in the work, the future studies associated with the DED assisted with UV are suggested as:

(1) Improving the heat dissipation of the ultrasonic equipment and seeking for the new high molten point materials as needle to solve the problem of overheating and dissolution of tungsten.

(2) The current work focus on the effect of the ultrasonic vibration on the performance of the parts along the scanning direction barely, another investigation into the effect of the ultrasonic vibrative on the anisotropy of parts needs to be performed in the future.

(3) In order to improve the accuracy of the model that simulates the fluid velocity and pressure distribution of the molten pool under ultrasonic vibration, the interaction between each layer needs to be considered in the simulation of the ultrasonic vibration on the solidification process of the molten pool.

5. Conclusion

In this work, the effect of ultrasonic vibration on 1Cr12Ni3MoVN alloy fabricated by directed energy deposition was studied by means of analyzing the microstructure and mechanical properties of the material with and without UV. In addition, the mechanism of ultrasound action in the molten pool was investigated through simulation, and the condition of the ultrasonic cavitation and the effect of the cavitation and acoustic streaming was also discussed based on the simulation results. The main conclusions can be summarized as follows:

(1) The proportion of columnar crystals in the samples decreases with increasing ultrasonic power. The microstructure is equiaxed crystal at the ultrasonic power of 1000 W. Besides, the interlayer grains are refined by UV with a decrease from 158 μm^2 at 0 W to 80 μm^2 at 1000 W.

(2) The microhardness of the samples raises after being treated with UV and then reduces with increasing ultrasonic power. The elongation of the samples with UV increases by 53.8% compared with that without UV, accompanied by an approximate ultimate tensile strength.

(3) With UV treatment, the pressure in the molten pool is from − 4.6 MPa to + 4.4 MPa, which is much larger than the cavitation threshold, and the cavitation effect can take place within almost the whole molten pool. Moreover, the shock waves with large local velocity and pressure created by the burst of cavitation bubbles impact the previously-grown grains into tiny grains and refine the grains. The maximum velocity of the molten pool caused by ultrasound reaches 2.6 m/s, reducing the temperature gradient, accelerating the solidification rate, and then increasing the nucleation rate. The product $G \times R$ increases and the ratio G/R decreases after UV treatment, therefore the fine equiaxed crystals form.

CRediT authorship contribution statement

Zhen Wang: Conceptualization, Investigation, Methodology, Formal analysis, Writing – original draft. **Fengchun Jiang:** Resources, Supervision, Writing – review & editing. **Chunhuan Guo:** Project administration, Writing – review & editing. **Xiaodong Xing:** Resources, Supervision. **Zhenlin Yang:** Investigation. **Haixin Li:** Data curation. **Chuanming Liu:** Investigation, Methodology. **De Xu:** Visualization. **Guorui Jiang:** Visualization. **Sergey Konovalov:** Writing – review & editing.

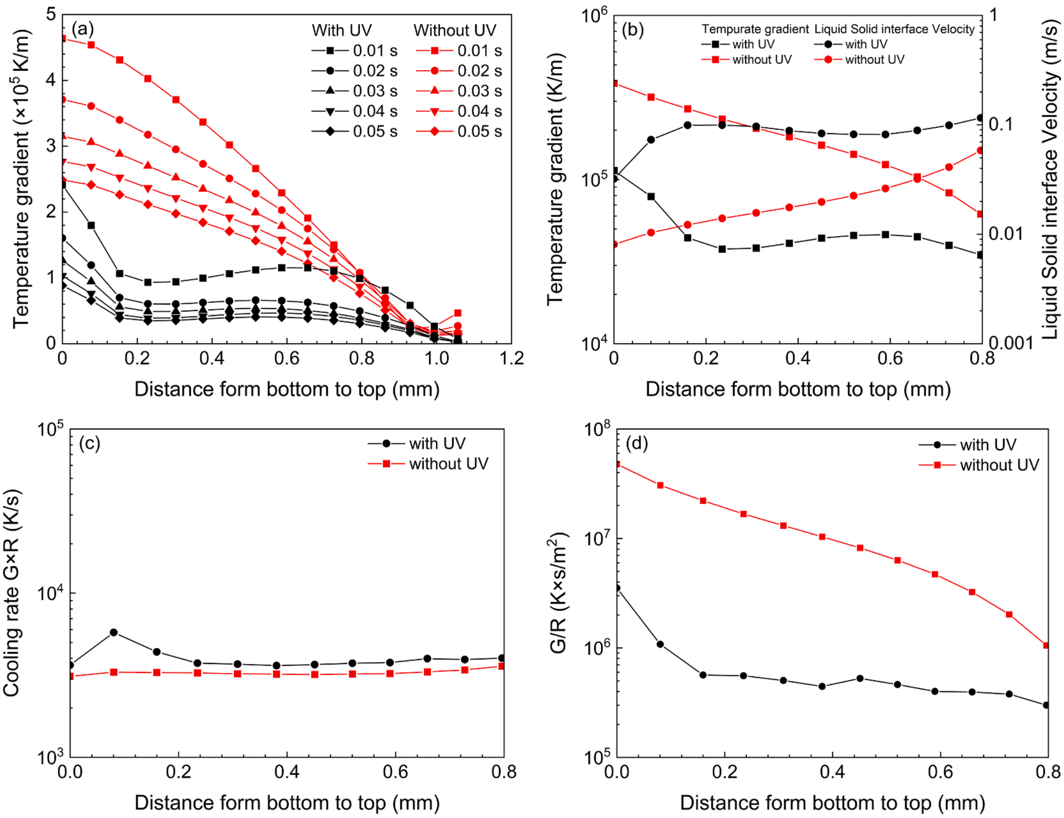

Fig. 14. Variation of temperature gradient and solidification rate during solidification: (a) Temperature gradient in the molten pool along Line 1 at different time, (b) Temperature gradient and solidification rate at the liquid–solid interface, (c) G × R and (d) G/R at the liquid–solid interface with and without UV treatment.

Declaration of Competing Interest

The authors declare that they have no known competing financial interests or personal relationships that could have appeared to influence the work reported in this paper.

Data availability

No data was used for the research described in the article.

Acknowledgments

This work was supported by the National Key R&D Program of China (No. 2021YFC2801904), the Science Fund of Shandong Laboratory of Advanced Materials and Green Manufacturing (Yantai) (No. AMGM2021F01), Fundamental Research funds for the Central Universities (No. 3072021CFT1012), and Leading Scientific Research Project of CNNC (No. KY90200210015), High-End Foreign Experts Introduction Program (No. G2021180004L), and China-Russia Joint Project of Harbin Engineering University (2021HEUCRF002).

References

[1] T. DebRoy, H.L. Wei, J.S. Zuback, T. Mukherjee, J.W. Elmer, J.O. Milewski, A. M. Beese, A. Wilson-Heid, A. De, W. Zhang, Additive manufacturing of metallic components – Process, structure and properties[J], Prog. Mater Sci. 92 (2018) 112–224.

[2] B. Li, H. Zheng, C. Han, K. Zhou, Nanotwins-containing microstructure and superior mechanical strength of a Cu-9Al-5Fe-5Ni alloy additively manufactured by laser metal deposition[J], Addit. Manuf. 39 (2021) 101825.

[3] M. Fang, Y. Han, Z. Shi, G. Huang, J. Song, W. Lu, Embedding boron into Ti powder for direct laser deposited titanium matrix composite: Microstructure evolution and the role of nano-TiB network structure[J], Compos. B Eng. 211 (2021) 108683.

[4] K.D. Traxel, A. Bandyopadhyay, Reactive-deposition-based additive manufacturing of Ti-Zr-BN composites[J], Addit. Manuf. 24 (2018) 353–363, https://doi.org/10.1016/j.addma.2018.10.005.

[5] T. Feldhausen, N. Raghavan, K. Saleeby, L. Love, T. Kurfess, Mechanical properties and microstructure of 316L stainless steel produced by hybrid manufacturing[J], J. Mater. Process. Technol. 290 (2021) 116970.

[6] H. Sohn, P. Liu, H. Yoon, K. Yi, L. Yang, S. Kim, Real-time porosity reduction during metal directed energy deposition using a pulse laser[J], J. Mater. Sci. Technol. 116 (2022) 214–223.

[7] H.L. Wei, G.L. Knapp, T. Mukherjee, T. DebRoy, Three-dimensional grain growth during multi-layer printing of a nickel-based alloy Inconel 718[J], Addit. Manuf. 25 (2019) 448–459.

[8] J. Ning, H.-B. Zhang, S.-M. Chen, L.-J. Zhang, S.J. Na, Intensive laser repair through additive manufacturing of high-strength martensitic stainless steel powders (I) –powder preparation, laser cladding and microstructures and properties of laser-cladded metals[J], J. Mater. Res. Technol. 15 (2021) 5746–5761.

[9] W. Chen, B.o. Xiao, L. Xu, Y. Han, L. Zhao, H. Jing, Additive manufacturing of martensitic stainless steel matrix composites with simultaneously enhanced strength-ductility and corrosion resistance[J], Compos. B Eng. 234 (2022) 109745.

[10] M. Qian, W. Xu, M. Brandt, H.P. Tang, Additive manufacturing and postprocessing of Ti-6Al-4V for superior mechanical properties[J], MRS Bull. 41 (10) (2016) 775–784.

[11] K. Benarji, Y. Ravi Kumar, A.N. Jinoop, C.P. Paul, K.S. Bindra, Effect of Heat-Treatment on the Microstructure, Mechanical Properties and Corrosion Behaviour of SS 316 Structures Built by Laser Directed Energy Deposition Based Additive Manufacturing[J], Met. Mater. Int. 27 (3) (2021) 488–499.

[12] S. Cheruvathur, E.A. Lass, C.E. Campbell, Additive Manufacturing of 17–4 PH Stainless Steel: Post-processing Heat Treatment to Achieve Uniform Reproducible Microstructure[J], JOM 68 (3) (2016) 930–942, https://doi.org/10.1007/s11837-015-1754-4.

[13] C.J. Todaro, M.A. Easton, D. Qiu, D. Zhang, M.J. Bermingham, E.W. Lui, M. Brandt, D.H. StJohn, M. Qian, Grain structure control during metal 3D printing by high-intensity ultrasound[J], Nat. Commun. 11 (1) (2020), https://doi.org/10.1038/s41467-019-13874-z.

[14] Z. Yang, L. Zhu, S. Wang, J. Ning, Y. Dun, G. Meng, P. Xue, P. Xu, B.o. Xin, Effects of ultrasound on multilayer forming mechanism of Inconel 718 in directed energy deposition[J], Addit. Manuf. 48 (2021) 102462.

[15] D. Yuan, S. Shao, C. Guo, F. Jiang, J. Wang, Grain refining of Ti-6Al-4V alloy fabricated by laser and wire additive manufacturing assisted with ultrasonic vibration[J], Ultrason. Sonochem. 73 (2021) 105472.

[16] L. Zhou, S. Chen, M. Ma, Jing liang, J. Chen, M. Wang, The dynamic recrystallization mechanism of ultrasonic power on non-contact ultrasonic-assisted direct laser deposited alloy steel[J], Mater. Sci. Eng. A 840 (2022) 142971.

[17] W. Cong, F. Ning, A fundamental investigation on ultrasonic vibration-assisted laser engineered net shaping of stainless steel[J], Int J Mach Tool Manu 121 (2017) 61–69, https://doi.org/10.1016/j.ijmachtools.2017.04.008.
[18] H. Wang, Y. Hu, F. Ning, W. Cong, Ultrasonic vibration-assisted laser engineered net shaping of Inconel 718 parts: Effects of ultrasonic frequency on microstructural and mechanical properties[J], J. Mater. Process. Technol. 276 (2020) 116395.
[19] D. Yuan, X. Sun, L. Sun, Z. Zhang, C. Guo, J. Wang, F. Jiang, Improvement of the grain structure and mechanical properties of austenitic stainless steel fabricated by laser and wire additive manufacturing assisted with ultrasonic vibration[J], Mater. Sci. Eng. A 813 (2021) 141177.
[20] F. Ji, X. Qin, Z. Hu, X. Xiong, M. Ni, M. Wu, Influence of ultrasonic vibration on molten pool behavior and deposition layer forming morphology for wire and arc additive manufacturing[J], Int. Commun. Heat Mass Transfer 130 (2022) 105789.
[21] N. Zong, M. Zhang, X. Liang, et al., Optimizing distance between laser and ultrasonic vibration points for additive manufacturing of HG785 steel with the assistance of ultrasonic vibration[J], J. Braz. Soc. Mech. Sci. Eng. 43 (9) (2021) 408, https://doi.org/10.1007/s40430-021-03133-y.
[22] X. Tian, Y. Zhu, C.V.S. Lim, J. Williams, R. Boyer, X. Wu, K. Zhang, A. Huang, Isotropic and improved tensile properties of Ti-6Al-4V achieved by in-situ rolling in direct energy deposition[J], Addit. Manuf. 46 (2021) 102151.
[23] W. Chen, L. Xu, L. Zhao, Y. Han, X. Wang, C. Hu, H. Jing, Application of hybrid additive manufacturing technology for performance improvement of martensitic stainless steel[J], Addit. Manuf. 51 (2022) 102648.
[24] B. Wang, D. Tan, T.L. Lee, J.C. Khong, F. Wang, D. Eskin, T. Connolley, K. Fezzaa, J. Mi, Ultrafast synchrotron X-ray imaging studies of microstructure fragmentation in solidification under ultrasound[J], Acta Mater. 144 (2018) 505–515.
[25] T. Yuan, S. Kou, Z. Luo, Grain refining by ultrasonic stirring of the weld pool[J], Acta Mater. 106 (2016) 144–154, https://doi.org/10.1016/j.actamat.2016.01.016.
[26] J. Mi, D. Tan, T.L. Lee, In Situ Synchrotron X-ray Study of Ultrasound Cavitation and Its Effect on Solidification Microstructures[J], Metall. Mater. Trans. B 46 (4) (2015) 1615–1619, https://doi.org/10.1007/s11663-014-0256-z.
[27] J.-W. Li, T. Momono, Y. Fu, Z. Jia, Y. Tayu, Effect of ultrasonic stirring on temperature distribution and grain refinement in Al-1.65%Si alloy melt[J], Trans. Nonferrous Met. Soc. Chin. 17 (4) (2007) 691–697.
[28] S. Shen, X. Song, Q. Li, X. Li, R. Zhu, G. Yang, A study on stress corrosion cracking and hydrogen embrittlement of Jethete M152 martensitic stainless steel[J], Mater. Sci. Eng. A 740-741 (2019) 243–251.
[29] H. Chae, E.-W. Huang, W. Woo, S.H. Kang, J. Jain, K.e. An, S.Y. Lee, Unravelling thermal history during additive manufacturing of martensitic stainless steel[J], J. Alloy. Compd. 857 (2021) 157555.
[30] M. Ghaffari, A. Vahedi Nemani, A. Nasiri, Microstructure and mechanical behavior of PH 13–8Mo martensitic stainless steel fabricated by wire arc additive manufacturing[J], Addit. Manuf. 49 (2022), 102374, https://doi.org/10.1016/j.addma.2021.102374.
[31] C. Tan, J.i. Zou, D.i. Wang, W. Ma, K. Zhou, Duplex strengthening via SiC addition and in-situ precipitation in additively manufactured composite materials[J], Compos. B Eng. 236 (2022) 109820.
[32] J. Samei, H. Asgari, C. Pelligra, M. Sanjari, S. Salavati, A. Shahriari, M. Amirmaleki, M. Jahanbakht, A. Hadadzadeh, B.S. Amirkhiz, M. Mohammadi, A hybrid additively manufactured martensitic-maraging stainless steel with superior strength and corrosion resistance for plastic injection molding dies[J], Addit. Manuf. 45 (2021) 102068.
[33] F. Khodabakhshi, M.H. Farshidianfar, A.P. Gerlich, M. Nosko, V. Trembošová, A. Khajepour, Effects of laser additive manufacturing on microstructure and crystallographic texture of austenitic and martensitic stainless steels[J], Addit. Manuf. 31 (2020) 100915.
[34] A. Hadadzadeh, A. Shahriari, B.S. Amirkhiz, J. Li, M. Mohammadi, Additive manufacturing of an Fe–Cr–Ni–Al maraging stainless steel: Microstructure evolution, heat treatment, and strengthening mechanisms[J], Mater. Sci. Eng. A 787 (2020) 139470.
[35] R. Cottam, J. Wang, V. Luzin, Characterization of microstructure and residual stress in a 3D H13 tool steel component produced by additive manufacturing[J], J. Mater. Res. 29 (17) (2014) 1978–1986, https://doi.org/10.1557/jmr.2014.190.
[36] O. Hentschel, L. Siegel, C. Scheitler, F. Huber, D. Junker, A. Gorunow, M. Schmidt, Processing of AISI H11 tool steel powder modified with carbon black nanoparticles for the additive manufacturing of forging tools with tailored mechanical properties by means of laser metal deposition (LMD)[J], Metals 8 (9) (2018) 659.
[37] M.J. Bermingham, D.H. StJohn, J. Krynen, S. Tedman-Jones, M.S. Dargusch, Promoting the columnar to equiaxed transition and grain refinement of titanium alloys during additive manufacturing[J], Acta Mater. 168 (2019) 261–274.
[38] Y.L. Hu, Y.L. Li, S.Y. Zhang, X. Lin, Z.H. Wang, W.D. Huang, Effect of solution temperature on static recrystallization and ductility of Inconel 625 superalloy fabricated by directed energy deposition[J], Mater. Sci. Eng. A 772 (2020) 138711.
[39] J. Kang, X. Zhang, S. Wang, J. Ma, T. Huang, The comparison of ultrasonic effects in different metal melts[J], Ultrasonics 57 (2015) 11–17.
[40] Y. Su, Z. Li, K.C. Mills, Equation to estimate the surface tensions of stainless steels [J], J. Mater. Sci. 40 (2005) 2201–2205, https://doi.org/10.1007/s10853-005-1933-8.
[41] F.R. Gilmore, The growth or collapse of a spherical bubble in a viscous compressible liquid[J], California Institute of Technology, 1952.
[42] J.C. Lippold (Ed.), Welding Metallurgy and Weldability, Wiley, 2015.